COMPACT, TUNABLE COMPTON SCATTERING GAMMA-RAY SOURCES*

F.V. Hartemann, F. Albert, G.G. Anderson, S. G. Anderson, A.J. Bayramian, S.M. Betts, T.S. Chu, R.R. Cross, C.A. Ebbers, S.E. Fisher, D. J. Gibson, A.S. Ladran, R.A. Marsh, M. J. Messerly, K.L. O'Neill, V. A. Semenov, M.Y. Shverdin, C.W. Siders, D.P. McNabb, and C.P.J. Barty, LLNL, Livermore, CA 94550, U.S.A.
A.E. Vlieks, E.N. Jongewaard, S.G. Tantawi and T.O. Raubenheimer, SLAC, Stanford, CA 94025, U.S.A.

Abstract

Recent progress in accelerator physics and laser technology have enabled the development of a new class of gamma-ray light sources based on Compton scattering between a high-brightness, relativistic electron beam and a high intensity laser pulse produced via chirped-pulse amplification (CPA). A precision, tunable gamma-ray source driven by a compact, high-gradient X-band linac is currently under development at LLNL. High-brightness, relativistic electron bunches produced by the linac interact with a Joule-class, 10 ps laser pulse to generate tunable γ-rays in the 0.5-2.5 MeV photon energy range via Compton scattering. The source will be used to excite nuclear resonance fluorescence lines in various isotopes; applications include homeland security, stockpile science and surveillance, nuclear fuel assay, and waste imaging and assay. The source design, key parameters, and current status are presented.

INTRODUCTION AND MOTIVATION

Recent work has been performed at LLNL to demonstrate isotope-specific detection of shielded materials via nuclear resonance fluorescence (NRF) using a tunable, quasi-monochromatic Compton scattering gamma-ray source operating between 0.2 MeV and 0.9 MeV photon energy. This technique is called Fluorescence Imaging in the Nuclear Domain with Energetic Radiation (or FINDER). This work has, among other things, demonstrated the detection of ^{7}Li shielded by Pb, utilizing gamma rays generated by a linac-driven, laser-based Compton scattering gamma-ray source developed at LLNL.

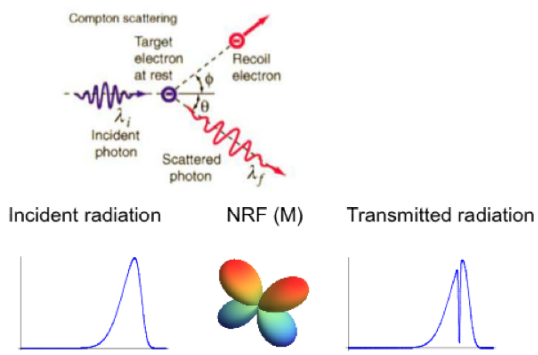

Figure 1: Compton scattering and NRF.

This program has also helped lay the theory and modeling foundations for isotopic imaging using NRF by benchmarking a complete suite of modeling codes against experiments, that can now be extended to address spatially-resolved, isotopic detection. The ability to produce isotope-specific images of unknown objects with deeply penetrating radiation will transform the special nuclear material (SNM) detection problem from simply identifying high optical depth cargo or high-Z materials to the unambiguous detection and verification of specific, dangerous contraband materials. The high spectral brightness and concurrent narrow bandwidth of this technology significantly reduces the radiological dose required for detection and largely eliminates artifacts due to small-angle elastic Compton scattering in the objects under interrogation. The highly-collimated, mono-energetic nature of the source also leads to simple detection protocols which can not only verify the presence of SNMs, but can also ascertain the absence thereof with a 99.9999% confidence level over a short interrogation time. Essentially, the phase space density of the gamma-ray beam used for interrogation or imaging is so high that discrimination against parasitic processes and backgrounds becomes both relatively simple to implement and highly effective.

The two key components of this powerful detection scheme are the Compton scattering gamma-ray source and the detection unit; more specialized aspects of the system range from fiber laser-driven electron photo-injectors; high-brightness, high-gradient electron linacs; and hyper-dispersion chirped-pulse amplification (CPA) lasers; to sub-picosecond laser-electron synchronization techniques; advanced γ-ray modeling; and highly sensitive detectors.

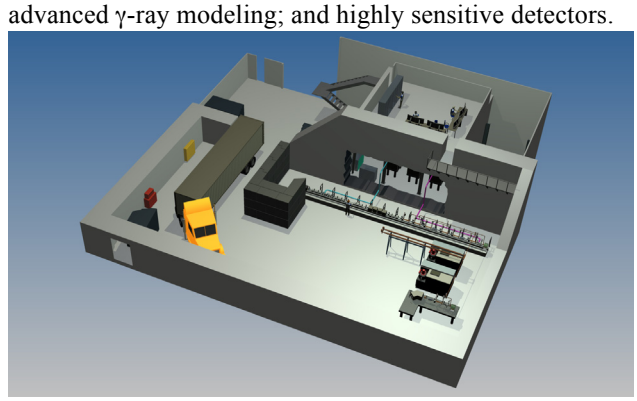

Figure 2: LLNL proposed Compton scattering γ-ray source facility.

The Laboratory is currently building a tunable, narrow-bandwidth, 3rd generation mono-energetic gamma-ray (MEGa-ray) source based on new high-gradient (> 65 MeV/m) X-band (11.424 GHz) rf accelerator structures capable of operating at 120 Hz, developed at SLAC (Stanford Linear Accelerator Center) and built in collaboration with SLAC; and laser technology developed for the previous T-REX (Thomson-Radiated Extreme X-Ray) source: a fiber-based photo-gun drive laser using frequency quadrupling and hyper-Michelson pulse shaping; and a 1 J, 10 ps, 120 Hz system using power amplification in diode-pumped Nd:YAG, operating near the Fourier transform limit with good beam quality, and utilizing proprietary LLNL hyper-dispersion stretching and compression technology. The compact accelerator also includes a custom, integrated focusing and transport lattice and interaction region designed to effectively shield parasitic x-ray production due to dark current. The facility is expected to produce γ-ray beams at a repetition rate of 120 Hz, with a peak brightness exceeding 10^{20} photons/(s x mm^2 x mrad^2 x 0.1% bandwidth).

COMPTON SCATTERING

This section is intended as a brief summary of the main properties of Compton scattering. The incident electron and photon 4-momenta are given by u_μ and k_μ; the scattered photon 4-wavenumber is q_μ, and the electron 4-velocity after the interaction satisfies energy-momentum conservation: $v_\mu = u_\mu + k_\mu - q_\mu$. From these parameters, the incident and scattered light-cone variables can be computed: $\kappa = u_\mu k^\mu$, $\lambda = u_\mu q^\mu$ [1]. In QED units, the Compton formula is:

$$\kappa - \lambda = k_\mu q^\mu. \tag{1}$$

Note that the term on the right-hand side corresponds to recoil; it is absent in formalisms based on Thomson scattering. The spin-independent component of the Lorentz-boosted Klein-Nishina differential cross-section [2] is:

$$\frac{d\sigma}{d\Omega} = \frac{\alpha^2}{2}\left(\frac{q}{\kappa}\right)^2 \left\{ \frac{1}{2}\left(\frac{\kappa}{\lambda}+\frac{\lambda}{\kappa}-2\right) + 2\left[\varepsilon_\mu \pi^\mu - \frac{(\varepsilon_\mu u^\mu)(\pi_\mu v^\mu)}{\kappa} + \frac{(\varepsilon_\mu v^\mu)(\pi_\mu u^\mu)}{\lambda}\right]^2 \right\}. \tag{2}$$

Here, ε_μ and π_μ correspond to the incident and scattered 4-polarizations. These quantities can then be used in conjunction with the phase space densities of the incident electrons and photons [3] to derive the spectral brightness of the source for a given scattering solid angle [4]. Typically, head-on collisions are considered because they yield the maximum relativistic Doppler upshift and minimal sensitivity to timing and synchronization; in such situations, one obtains spectra that are accurately described by the product of a Gaussian and an error function (for Gaussian phase space distributions). Using the full electron beam phase space as an input to the simulations yields more detailed spectra, as illustrated in Fig. 3. In general, the asymmetric low energy contribution on-axis can be traced back to the electron beam emittance, which results in a distribution of crossing angles at focus: some electrons do not contribute their maximum Doppler upshift in the direction of observation.

In the case where the laser spectrum is narrow compared to other parameters ($\Delta\gamma/\gamma, \varepsilon_n$), brightness simulations can be performed efficiently by calculating the following quantities for each macro-particle:

$$\frac{r_0^2}{\sqrt{\pi} q \left(\gamma + u_z\right)^2 \Delta k}, \quad e^{-\left(k_0 - q\frac{\gamma+u_z}{\gamma-u_z-2q}\right)^2/\Delta k^2}; \tag{3}$$

and replacing them by a Dirac delta-function with position and integral,

$$q = k_0 \frac{\gamma - u_z}{\gamma + u_z + 2k_0}, \quad \frac{r_0^2}{\left(\gamma + u_z\right)^2 k_0}. \tag{4}$$

In the specific case of Eqs. (3) and (4), the scattered radiation is on-axis, and the laser spectrum is a Fourier transform-limited Gaussian.

The calculation is finalized by calculating the dose radiated by each macro-particle, with total cross-section $N_e\sigma/N$, where N_e is the number of electrons and N is the number of macro-particles; by summing incoherently over all macro-particles; and by binning the result along the scattered frequency axis.

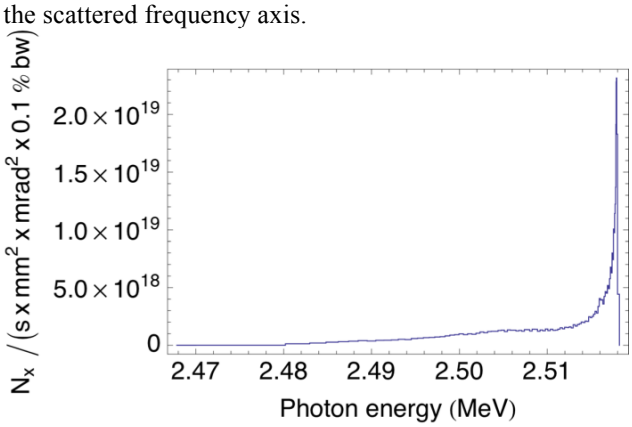

Figure 3: Typical on-axis spectral brightness (see Table 1).

In Fig. 4, the electron beam focal spot size is varied, while the laser parameters are fixed, in order to determine how the total dose decreases when the beams are not properly matched. In conjunction with this optimization process, one must keep in mind the fact that, as the electron beam focusing increases, so does the γ-ray beam divergence; as a result the optimum brightness is obtained for an electron beam size of 25 μm, as shown in Fig. 5.

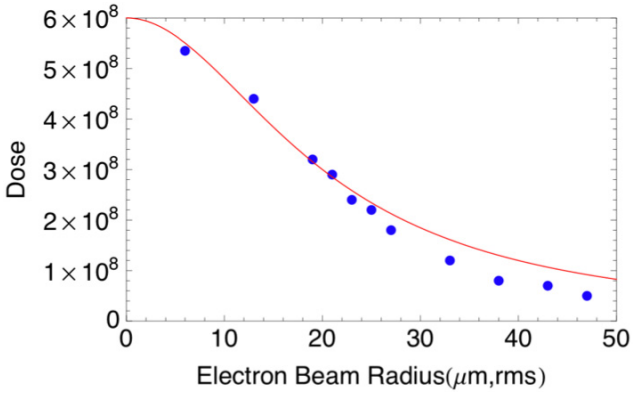

Figure 4: Dose as a function of electron beam radius.

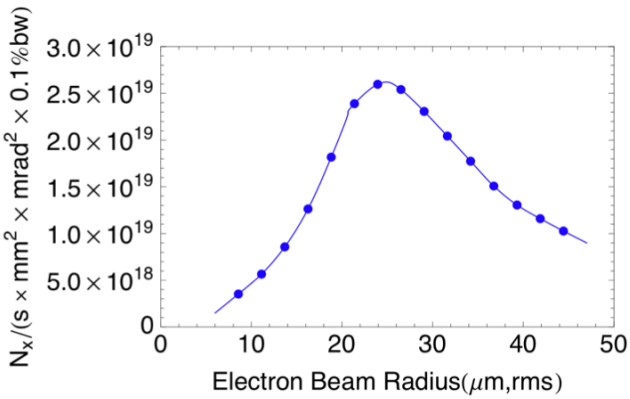

Figure 5: Brightness optimization.

T-REX NRF RESULTS

The principal properties (beam profile and spectrum) of the source are those of a Compton scattering source: The beam is well collimated (10.4 x 6 mrad^2), and the peak energy of the spectrum varies with $\approx 4\gamma^2\hbar\omega$, where γ is the electron relativistic factor and $\hbar\omega$ is the laser photon energy. Furthermore, spectra recorded on LN_2 cryo-cooled high-purity Ge detectors by scattering the beam off an Al plate agree very well with Monte-Carlo simulations performed with the MCNP 5 code and with a relative spectral width of 12 %.

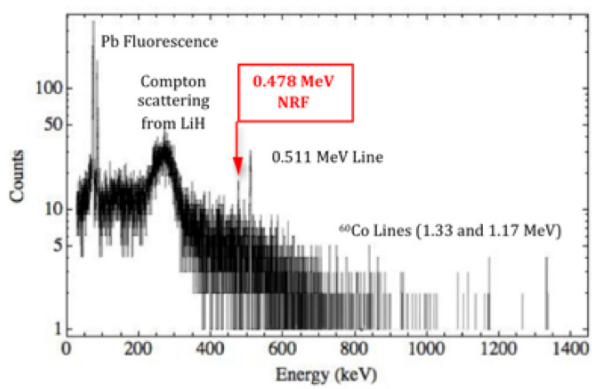

Figure 6: Full spectrum on HPGe detector.

We have used the source to detect the 0.478 MeV NRF line of ^{7}Li in a LiH target, experiment for which the laser wavelength was 532 nm and the electron beam energy 116 MeV. A 8 cm long LiH sample with a 0.36 g/cm^3 density was placed in the beam path, 20 m away from the interaction region, and the NRF scattered photons were detected by another germanium detector 15 cm away from the target and oriented at 90^o with respect to the incident beam axis. The resulting spectrum is displayed on Fig. 5 where, along with the 0.478 MeV line of ^{7}Li, several characteristic lines resulting from the interaction arise. With this experiment, we have shown that the high brightness and narrow bandwidth of laser-based Compton scattering sources will provide a unique specific isotope detection capability.

X-BAND LINAC

The high brightness electron linac is a key component of the facility. Design criteria include rf phase and amplitude stability, high-gradient operation at 120 Hz, and low emittance at the interaction point.

X-Band rf Gun

The emittance-compensated gun design used for this linac is very similar to the X-band rf gun developed by Vlieks and collaborators [5], with improved field balance and mode separation; it will generate 7 MeV photo-electron bunches with 0.4 nC charge and approximately 1 mm.mrad normalized emittance after compensation in a solenoid field of 7 kG and a drift of 0.75 m.

Photocathode Laser

To generate the electrons at the injector photocathode, a 263 nm laser pulse, shaped in time and space to have a uniform cylindrical profile, is used. This pulse is generated from an all-fiber front end, which provides up to 1 mJ, 1053 nm pulses that are frequency quadrupled, replicated and stacked to generate the desired temporal profile, and clipped to produce the necessary spatial profile. A full description of the laser system is presented in Ref. [6].

High-Power X-Band rf

Approximately 400 MW of compressed X-band rf power will be available to energize the gun and linac. This power will be produced by 2 XL-4 klystrons, each generating 50 MW, 1.6 μs pulses at up to 120 Hz repetition rate; a SLED II cavity will then produce 400 MW, 400 ns pulses. Stability of the rf is paramount, and begins with the HV modulators; to this end solid-state technology combined with high transformer ratios is being considered to drive the klystrons.

Linac

The so-called T53VG3(MC) sections will be used to accelerate the beam up to 250 MV; these sections have demonstrated excellent beam dynamics characteristics, as well as high gradient operation (> 65 MV/m). The linac architecture is shown in Fig. 7, and includes a small chicane to mitigate near-axis halo Bremsstrahlung.

INTERACTION LASER

The interaction laser system is a crucial component of the machine; stability, robustness, and beam quality are important criteria for the technology choices used in its design. The system uses hyper-dispersion chirped-pulse amplification (HDCPA); pointing and stabilization feedback loops, a fiber front-end, and interferometrically stabilized beam transport to the interaction region.

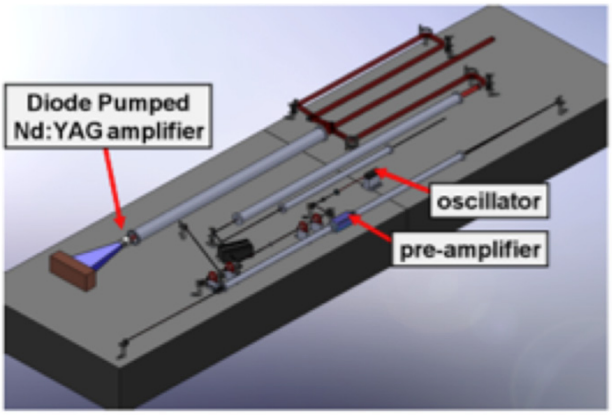

Figure 8: 10 J, 120-Hz interaction laser system.

120 Hz, 10 J Diode-Pumped Amplifier

A 10 J, 120 Hz Injection Laser System (10HILS) has been designed to enable photon interaction with nearly all electrons in the accelerator beamline. The 10HILS provides over 120 x the average power of the original T-REX injection laser system. The 10HILS is based upon diode-pumped solid-state laser expertise and technology developed on the Mercury laser project and the Tailored Aperture Ceramic Laser (TACL). Diode pumping is utilized to decrease the thermal load on amplifier slabs, while increasing efficiency and system reliability. The master oscillator – power amplifier architecture starts with a 30 μJ stretched pulse from the front end laser system, which is pre-amplified to the 100 mJ level, then image relayed to the four-pass Nd:YAG power amplifier. The 10HILS power amplifier is a layered Nd:YAG/sapphire composite, which allows aggressive thermal management and parasitic suppression in a single compact slab.

Table 1: Source Parameters.

Parameter	Linac	Laser
Energy/Wavelength	250 MeV	532 nm
Charge/Energy	0.25-0.4 nC	0.25 J
Duration	4 ps	10 ps
Focal spot	20 μm	20 μm
$\Delta\gamma/\gamma$ /Bandwidth	0.1%	0.4 nm
Emittance/*f*-#	0.3-1.0 mm.mrad	20/50
Repetition rate	120 Hz	120 Hz

REFERENCES

[1] L.M. Brown & R.P. Feynman, Phys. Rev. 85, 231 (1952).
[2] G. Bhatt *et al*., Phys. Rev. A28, 2195 (1983).
[3] E. Wigner, Phys. Rev. 40, 749 (1932).
[4] F.V. Hartemann *et al*. Phys. Rev. STAB 8, 100702 (2005).
[5] A.E. Vlieks *et al*., *High Energy Density & High Power RF: 6th Workshop*, 358 (2003).
[6] D. Gibson *et al*., PAC Proceedings, TU6RFP047 (2009).

*This work is performed under the auspices of the U.S. DoE by LLNL under Contract DE-AC52-07NA27344 and supported by DNDO CFP06-TA-02-LL12.

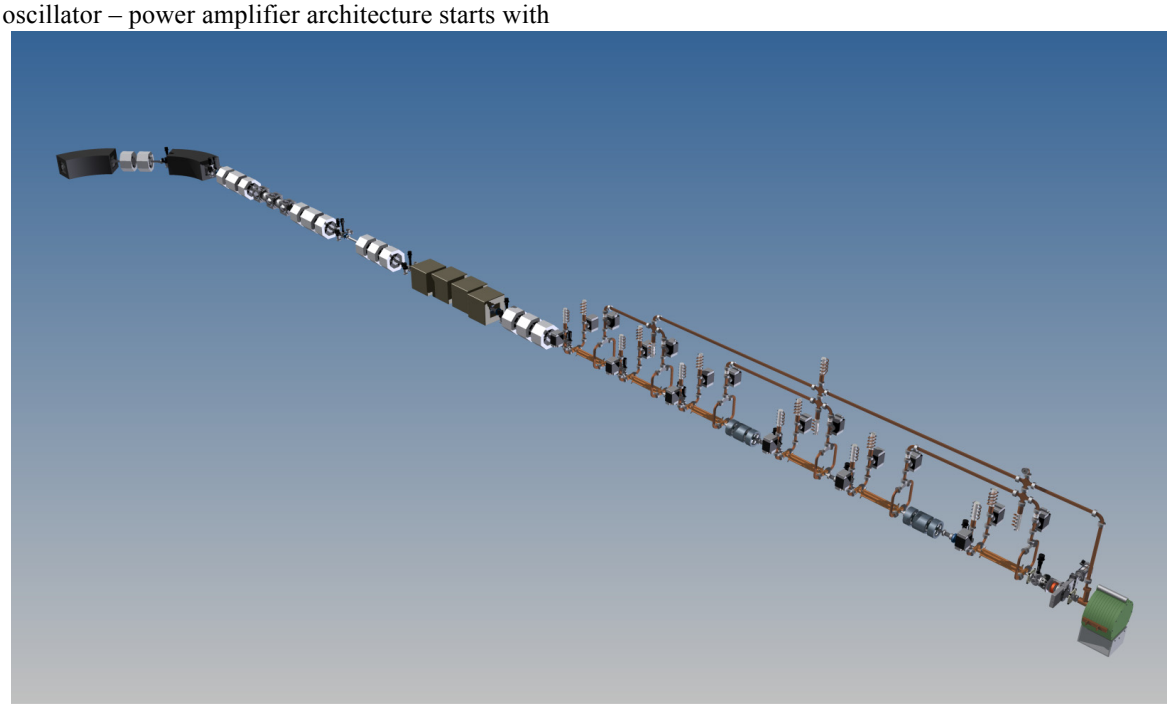

Figure 7: X-band linac architecture.